

## RESEARCH ARTICLE

# Compact Quad-Band CP Series-Fed Circular Slit Microstrip Array Antenna Using Machine Learning

BUDHADEB MAITY<sup>1</sup> AND SISIR KUMAR NAYAK<sup>1,2</sup>, (Senior Member, IEEE)

<sup>1</sup>School of Energy Science and Engineering, IIT Guwahati, Guwahati 781039, India

<sup>2</sup>Department of Electronics and Electrical Engineering, IIT Guwahati, Guwahati 781039, India

Corresponding author: Budhaddeb Maity (maity176151008@iitg.ac.in)

**ABSTRACT** This article presents the design and characterization of a dual-band, compact, and dual-circularly polarized (CP) traveling wave series-fed circular slit microstrip array (TWSCSMA) antenna operating in quad-band CP at 2.5/3.5/3.8 GHz WiMAX and 5.2 GHz WLAN applications. The radiating structure consists of an annular ring traveling wave series-fed circular slit array elements, rotates in sequence with seven circular quasi-lumped resonators contributes to two-impedance bandwidth (IBW) and quad CP bands. The four split-ring resonators with double-annular rings are introduced on the defected ground plane to improve the impedance matching, IBW, and axial ratio bandwidth (ARBW) effectively. The measured results show that the proposed dual-CP TWSCSMA antenna yields two  $S_{11} \leq -10$  dB IBW of 33.85% and 50.73% and four < 3 dB ARBW of 16.26%, 12.52%, 8.22%, and 13.82% for port 1. Furthermore, modern machine learning regression techniques are used to improve the accuracy of the model performance requirements for the optimal design of the proposed antenna. The TWSCSMA antenna demonstrates a compact, low profile, wide impedance bandwidth, and minimum axial ratio which is making it a good candidate for WiMAX and WLAN applications.


**INDEX TERMS** Circularly polarized, axial ratio bandwidth, impedance bandwidth, defected ground structure, microstrip array, series-fed circular slit.

## I. INTRODUCTION

Recently, due to the increasing demands for modern wireless communication systems, the research on small and microstrip antenna arrays, radiating elements, feeding structures, and polarizations have attracted enormous attention. Due to its advantages of overcoming multipath fading, non-line-of-sight applications, and providing better mobility compared to linearly polarized antennas, the circularly polarized (CP) antenna is getting popular in wireless communication systems. In recent years, many researchers are designing CP antennas as well as minimizing the size using different techniques [1], [2], [3], [4]. The operating principle of CP antennas is to excite two orthogonal modes with equal amplitude and in-phase quadrature. This can be

achieved by introducing different techniques to design the multi-band CP antennas which will be applied to various communication systems, such as global positioning systems (GPS) and satellite communications [5], [6], [7], [8], [9]. The dual-band CP antennas have been proposed with a single feed, cavity-backed square annular slot [5], truncated corner square slots loaded with a set of split-ring resonators [6], and S-shaped slot center of the square radiator [7]. The single-feed microstrip patch antennas with the annular-ring slot on the square radiator or  $4 \times 4$  arrays with  $90^\circ$  phase difference power dividers have also been demonstrated for dual-band applications [8], [9]. Although these antennas generate a CP wave in their two bands, the antenna size is increased and 3 dB axial ratio bandwidths (ARBW) is narrowed.

Furthermore, single-feed microstrip patch antennas with loading stubs and etching slots on the square patch or

The associate editor coordinating the review of this manuscript and approving it for publication was Hussein Attia .

multistacked patches with a slit have also been discussed for triple-band applications [10], [11]. However, these single-feed CP patch antennas have less than 3.5% ARBW with the large size discussed. In [12], multiple L-shaped slits on the hexagonal slot as a radiator is proposed and triple CP bands i.e., 1.7%, 3.86%, 5.23% are achieved. In [13], a square slot with the metallic strips and split-ring resonator configuration, the 3 dB ARBW improved are presented. Though these antennas had small sizes the ARBW were still less than 11%. Recently, a quad-band CP antenna has been reported in [14], using inverted-U-shaped radiators and the ARBW of 5.4%, 8.3%, 3.7%, and 2.9% are achieved.

Among the various established techniques to design an antenna array, the sequential rotation technique (SRT) is found to be effective for CP array antenna in terms of improving the array’s bandwidth, radiation patterns, and polarization purity. Several designs of CP array antenna have been discussed, but the SRT is one of the most popular methods investigated in the literature to generate the CP operation [15], [16], [17], [19]. In an SRT, phase shiftings of 90° and 180° are achieved by applying λ/4 transmission lines with an L-shaped radiator [15]. A series feed network is reported [16], consisting of λ/4 transformer sections and adding an L-shaped ground strip in the radiator array to reduce cross-polarization. In [17], [18], and [19], the array elements are fed by different feeding networks like rat-race, Wilkinson power divider, and microstrip line. However, antenna configurations of these designs are usually large and the uses of a complex feeding network structure complicate the fabrication of the antenna. The antennas mentioned above are either thick in profile or large in aperture size, which motivates us to develop a compact multi-band CP antenna to some extent as well as improved the ARBW and IBW with maintain the minimum axial ratio using a series-fed circular slit array patch.

In this work, a new design of dual-CP TWSCSMA antenna effectively deals with a novel series-fed circular slit microstrip array which involves a compact annular ring TWSCSMA antenna with four split-ring resonators (SRR) unit cells with a double-annular ring on the defected ground plane. The proposed dual-CP TWSCSMA antenna has a distinct separation of the four CP bands (ARBW of 16.26%, 12.52%, 8.22%, and 13.82%) with improved operational impedance bandwidth (IBW of 33.85% and 50.73%) and minimum axial ratio (< 1.2 dB). Since the proposed antenna is electrically small, the achieved gain is low. However, the size of the antenna is compact with wide band IBW and ARBW characteristics. The machine learning regression (MLR) algorithm is used to predict the accurate model performance requirements of the dual-CP TWSCSMA antenna for desired two IBW and four wide ARBW. The parameters of the dual-CP TWSCSMA antenna obtained using CST Microwave Studio are validated with the experimental results.

This work is organized as follows: Section II discusses the optimized parameters of the antenna design, SFA configuration, design evolution, and current distribution analysis.

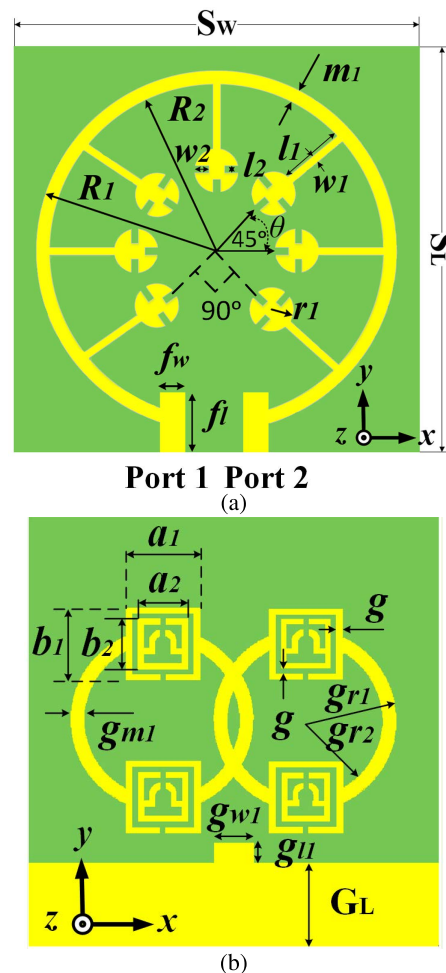


FIGURE 1. Geometry of dual-CP TWSCSMA antenna (a) top and (b) bottom view.

TABLE 1. Geometric parameters values.

Parameter	Value [mm]	Parameter	Value [mm]	Parameter	Value [mm]
$S_L$	41	$w_1$	0.4	$G_L$	8.2
$S_W$	41	$w_2$	0.4	$g_{w1}$	3.4
$R_1$	19	$l_1$	12.4	$g_{l1}$	2
$R_2$	18.2	$l_2$	0.7	$g_{r1}$	9
$m_1$	0.8	$a_1$	7	$g_{r2}$	8
$f_w$	2.2	$b_1$	7	$g_{m1}$	1
$f_l$	6.9	$a_2$	5	$g$	0.5
$r_1$	2.2	$b_2$	5	$h$	2.0

In Section III, the MLR algorithm models are discussed. The simulation, experimental results, and discussion are presented in Section IV. The conclusions are drawn in Section V.

## II. ANTENNA DESIGN AND ANALYSIS

### A. ANTENNA CONFIGURATION

The geometry of the compact dual-CP TWSCSMA antenna top view is illustrated in Fig. 1(a). As shown in Fig. 1(a), the proposed antenna is fed by a 50 Ω microstrip-fed printed on

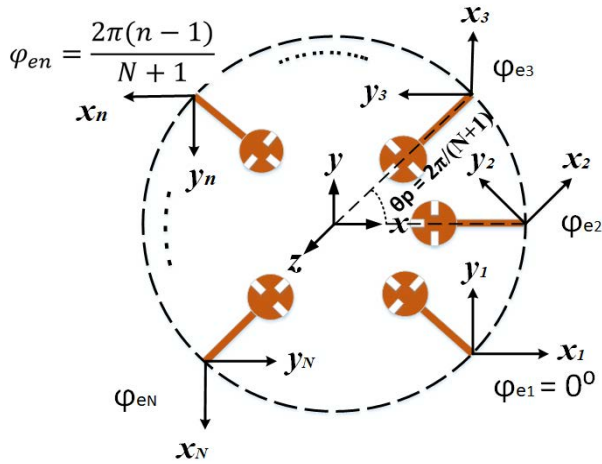


FIGURE 2. Configuration of  $N$  element of SCSA.

top of the 2 mm-thick FR-4 substrate having  $\epsilon_r = 4.3$  and loss tangent ( $\tan\delta$ ) = 0.025. In this figure, seven series-fed circular slit array elements in an annular ring are placed at an angle of  $45^\circ$  from each other. The bottom of the TWSCSMA antenna consists of four SRR unit cells with a double-annular ring on the defected ground structure (DGS) as shown in Fig. 1(b). The values of all the geometrical dimensions corresponding to Fig. 1 are shown in Table 1.

The four SRR unit cells ( $a_1 = b_1 = 7$  mm) with double-annular rings (outer radius  $g_{r1} = 9$  mm and inner radius  $g_{r2} = 8$  mm) are introduced in the ground plane to improve the operational bandwidth and minimize the axial ratio. To realize the left-hand circular polarization (LHCP) wave, the input RF signal for port 1 has a  $45^\circ$  phase increment in the clockwise direction. Similarly, to get the right-hand circular polarization (RHCP) wave, port 2 is fed with a phase increment of  $45^\circ$  in an anticlockwise direction for each circular slit patch. Using this concept, we can realize dual-CP radiation.

### B. THEORETICAL ANALYSIS OF CIRCULAR POLARIZATION GENERATION

Fig. 1(a) shows the circular slit patches arranged in a concentric ring fashion which is fed in series with the proper phase shifts. Seven circular slit patches are rotated sequentially by  $45^\circ$  and fit in an annular ring radiator that has an outer radius  $R_1 = 19$  mm and inner radius  $R_2 = 18.2$  mm.

To understand the polarization of the proposed antenna, an  $N$  number of uniform series-fed circular slit array (SCSA) elements as shown in Fig. 2 are fed from port 1 or port 2 to get LHCP or RHCP waves respectively. The radiation elements are symmetrically distributed around the  $z$ -axis so that the angle  $\theta_p$  between adjacent elements is  $2\pi/(N + 1)$ . It is assumed that each element is fed with uniform amplitude with an excitation current phase of the  $n^{th}$  element  $\varphi_{en}$ . The parameters shown in Fig. 2 are expressed as:

$$\theta_p = 2\pi/(N + 1) \tag{1}$$

$$\varphi_{en} = -\frac{2\pi(n - 1)}{N + 1}, \quad 1 \leq n \leq N = 7 \tag{2}$$

$$\begin{bmatrix} \hat{x}_n \\ \hat{y}_n \end{bmatrix} = \begin{bmatrix} \cos(\theta_p(n - 1)) & \sin(\theta_p(n - 1)) \\ -\sin(\theta_p(n - 1)) & \cos(\theta_p(n - 1)) \end{bmatrix} \begin{bmatrix} \hat{x} \\ \hat{y} \end{bmatrix} \quad (1 \leq n \leq N) \tag{3}$$

A plane wave propagates in the  $z$ -direction can have both  $x$  and  $y$  components of the electric field as expressed below:

$$E = (\hat{x}E_x + \hat{y}E_y)e^{-jkz} \tag{4}$$

The E-field ( $E$ ) on the sequentially rotated patches as shown in Fig. 2 can be decomposed into an RHCP component  $E_{RHCP}$  and an LHCP component  $E_{LHCP}$  as expressed below:

$$E = |E_{RHCP}|(\hat{x}_n - j\hat{y}_n) + |E_{LHCP}|(\hat{x}_n + j\hat{y}_n) \tag{5}$$

Since the circular array is rotationally symmetric,  $E_{RHCP}$  is equal for different radiation elements. It is also true for  $E_{LHCP}$ . Therefore, the resultant  $E_{RHCP}$  and  $E_{LHCP}$  are expressed as:

$$\begin{aligned} & \sum_{n=1}^N E_{RHCPn} e^{j\varphi_{en}} \\ &= \sum_{n=1}^N |E_{RHCPn}| (\hat{x}_n - j\hat{y}_n) e^{j\varphi_{en}} \\ &= \sum_{n=1}^N |E_{RHCPn}| (\hat{x} - j\hat{y}) e^{j\theta_p(n-1)} e^{j\varphi_{en}} \end{aligned} \tag{6}$$

$$\begin{aligned} & \sum_{n=1}^N E_{LHCPn} e^{j\varphi_{en}} \\ &= \sum_{n=1}^N |E_{LHCPn}| (\hat{x}_n + j\hat{y}_n) e^{j\varphi_{en}} \\ &= \sum_{n=1}^N |E_{LHCPn}| (\hat{x} + j\hat{y}) e^{-j\theta_p(n-1)} e^{j\varphi_{en}} \end{aligned} \tag{7}$$

The AR of the proposed antenna is given as

$$AR_{dB} = 20 \log_{10} \frac{|E_{RHCP}| + |E_{LHCP}|}{|E_{RHCP}| - |E_{LHCP}|} \tag{8}$$

The above expression is based on the boresight at the center of the ring being the origin of the spherical coordinate system.

### C. DESIGN EVOLUTION AND CP MECHANISM

The different design steps and their configurations are shown in Fig. 3 to understand the CP performance of the antenna. The different antennas are simulated using CST Microwave Studio software. The circular radiators are very popular because they are simple to fabricate and have small cross-polarization radiation [20], [21]. Therefore, the design starts with an annular ring radiator of radius  $R_1 = 19$  mm and  $R_2 = 18.2$  mm as shown in ANT 1 of Fig 3. Due to the increased current path in an annular ring, wider IBW and ARBW compared to circular patches [22] are achieved. For a

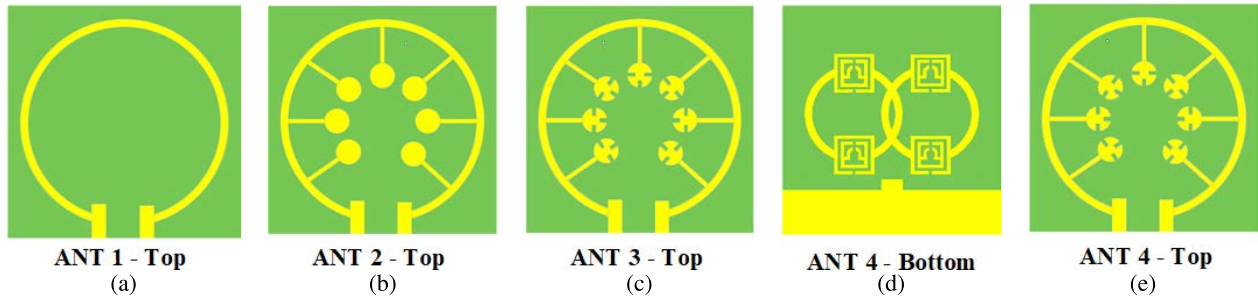


FIGURE 3. Evolution of the dual-CP TWSCMA antenna.

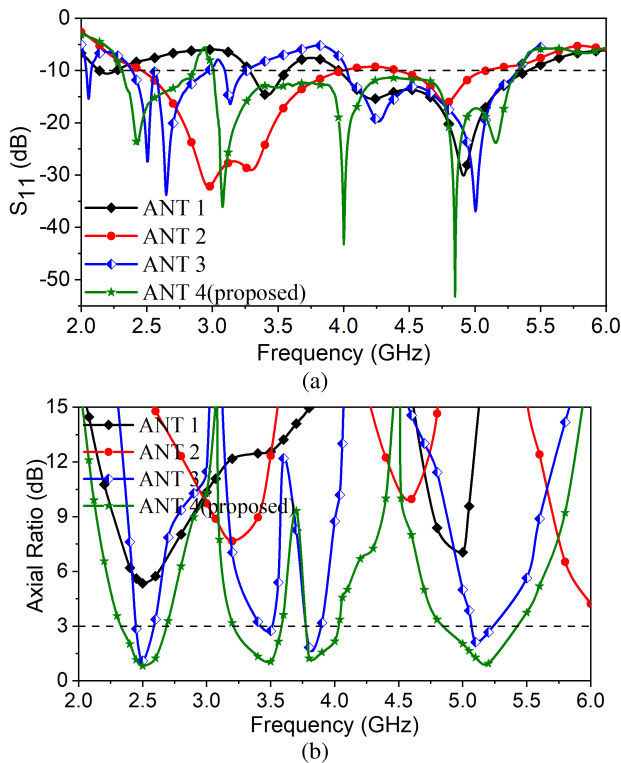


FIGURE 4. Evaluations of simulated (a)  $S_{11}$  and (b) AR of the proposed TWSCMA antenna.

traditional annular ring patch antenna, the  $TM_{11}$  mode is the fundamental resonant mode,  $\lambda_g$  is the wavelength of the lower resonating frequency  $f_g$  that can be expressed as follows:

$$\lambda_g = \frac{c}{f_g \sqrt{\epsilon_{eff}}} \quad (9)$$

where  $\epsilon_{eff}$  is the effective dielectric constant. As seen in Fig. 1(a), the mean circumference of a series-fed annular ring equals the wavelength at nearly the first resonant frequency [23]. The resonant frequency is calculated as follows:

$$f_{11} \approx \frac{c}{\pi(R_1 + R_2)} \left( \frac{1 + \epsilon_r}{2\epsilon_r} \right)^{\frac{1}{2}} \quad (10)$$

where  $f_{11}$  is the resonant frequency and  $\pi(R_1 + R_2)$  is the mean circumferences of the annular ring of the ANT 1. Based

on the detail parameters, the calculated resonance frequency is approximately  $f_{11} = 2.17$  GHz.

To clarify the proposed antenna performance process, the IBW and ARBW performances of ANT 1-ANT 4 have been compared in Fig. 4. It is noticed in Fig. 4(a) that the simple annular structure ANT 1 has two narrow impedance bands below -10 dB about 3–3.5 GHz and 3.7–5.53 GHz. However, it is linearly polarized. The ARBW is greater than 15 dB in two frequencies within the bandwidth as shown in Fig. 4(b). CP is generated by two orthogonal  $E$  vectors ( $E_{HOR}$ ,  $E_{VER}$ ) with equal amplitude and  $90^\circ$  phase difference, where  $E_{HOR}$  and  $E_{VER}$  represent the complex voltage in the horizontal and vertical planes, respectively.

The seven symmetrical circular slit patches of radius ( $r_1 =$ ) 2.2 mm are added as series-fed on the annular ring patch of ANT 1 so that the  $S_{11}$  performance shows an improvement in lower and decrease upper frequency in terms of bandwidth. This may be due to the increased current path induced by the horizontal annular ring. More importantly, the ARBW also drops significantly from about 15 dB to around 8 dB at 3.2 and 4.5 GHz.

In ANT 3, three rectangular slits (size:  $l_2 = 1.7$  mm and  $w_2 = 0.4$  mm) placed by  $90^\circ$  from each other are introduced in each of seven circular slit patches which act as the quasi-lumped-resonators (QLR) [19]. When QLRs are introduced in ANT 2 which is a linear polarized (LP) antenna with different radiated phases of  $90^\circ$ , the total radiated field in the  $z$ -direction of wave propagation can be expressed as follows:

$$\begin{aligned} E &= E_{ANT} + E_{QLR} \\ &= \frac{E_o}{2} e^{-jkz} [(1 + j)\hat{x} + (1 - j)\hat{y}] \end{aligned} \quad (11)$$

where  $E_{ANT}$  and  $E_{QLR}$  are the radiated field by a series-fed annular-ring antenna and QLRs respectively. Since both the radiated fields are perpendicular and magnitudes are the same, the CP radiation pattern is obtained. The position and dimensions of the QLRs i.e.,  $l_2 = 1.7$  mm and  $w_2 = 0.4$  mm of the ANT 2 are optimized to obtain the quad-band CP characteristics at the intended frequencies of 2.5, 3.5, 3.8, and 5.2 GHz. The  $S_{11}$  performance shows better improvement in lower and upper frequencies in terms of bandwidth. The ARBW also drops significantly from about 8 dB to around

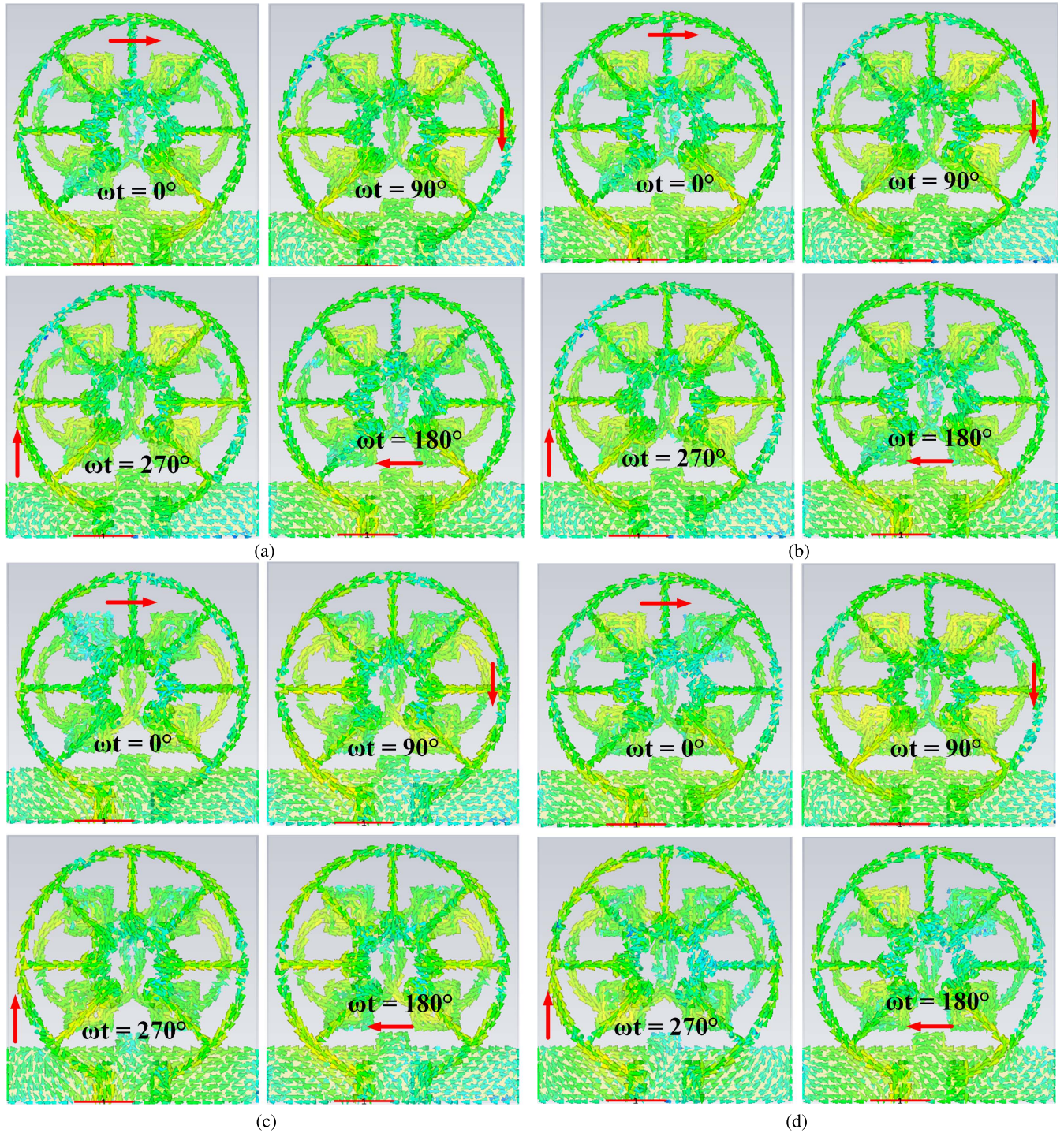


FIGURE 5. Surface current distributions at (a) 2.5, (b) 3.5, (c) 3.8 and (d) 5.2 GHz for port 1.

2 dB at 2.5, 3.5, 3.8, and 5.2 GHz. However, at this stage, the antenna does not possess wide IBW and CP characteristics.

For further improvement in IBW, ARBW, and better impedance matching, four SRR unit (area of  $49 \text{ mm}^2$  ( $7 \text{ mm} \times 7 \text{ mm}$ )) cells with double-annular rings are loaded with ANT 3 such that its position on the ground plane allows neutralizing unwanted surface coupling waves on the radiator as

shown in ANT 4. In the transmission line model of the SRR, L and C values determine the frequency of operation of the proposed antenna [24]. The length ( $b_1, b_2$ ) and width ( $a_1, a_2$ ) of the unit cells are adjusted to ensure  $90^\circ$  phase difference between the field components so that the bandwidths (IBW, ARBW) are significantly improved in ANT 4 as shown in Fig. 4. As a result, a compact dual-CP TWSCSMA antenna

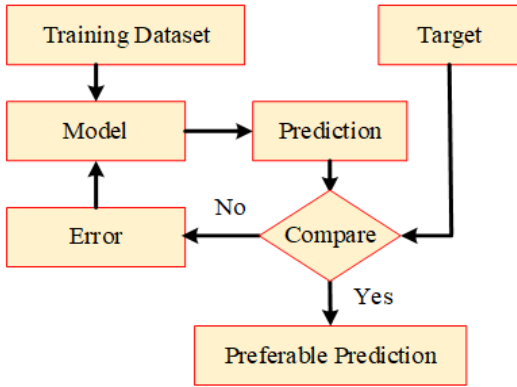


FIGURE 6. Perspective of MLR work.

achieves two wide -10 dB IBW from 2.213 to 2.982 GHz (29.62%) and from 3.071 to 5.342 GHz (53.81%) and less than 3 dB in four CP bands of 15.23% (2.382–2.723 GHz), 12.80% (3.213–3.652 GHz), 9.02% (3.741–4.092 GHz), and 11.65% (4.754–5.342 GHz) when it is excited either in port 1 or port 2.

**D. CURRENT DISTRIBUTION ANALYSIS**

The simulated current distribution of CP bands are studied at phases  $\omega t = 0^\circ$ ,  $\omega t = 90^\circ$ ,  $\omega t = 180^\circ$  and  $\omega t = 270^\circ$  as shown in Fig. 5(a)–5(d) at frequencies of 2.5, 3.5, 3.8, and 5.2 GHz respectively for port 1. It is observed that as the phase changes by  $90^\circ$ , the current distribution vector at all the resonant frequencies rotates clockwise +z-direction. Hence, the LHCP is obtained at the CP bands for port 1. And also, it is observed that the current reverses its direction when the feeding port is changed to port 2 hence, the RHCP is obtained at the four CP bands for this configuration.

**III. ANTENNA PARAMETER OPTIMIZATION USING MLR**

The purpose of using machine learning regression (MLR) algorithms in antenna modeling is to predict new model parameters using the training data set generated by the computational EM model [25] and to evaluate the model’s accuracy and generalization [26]. It can be realized by the input  $x$  and the corresponding output  $y$  parameters by connecting a model such that

$$y = M(x) \tag{12}$$

where  $y \in Y \subset \mathbb{R}^u$ , while  $u$  are the values of an output variable and  $x \in X \subset \mathbb{R}^c$ ,  $c$  are the values of input modeling variables. The accuracy can be expressed as a function of the mean squared error (MSE) function:

$$MSE = \frac{1}{N} \sum_{i=1}^N (y_i^{pred} - y_i^{meas})^2 \tag{13}$$

where  $y_i^{pred}$  is the predicted value,  $y_i^{meas}$  is the measured value and  $N$  number of data samples.

The performance of the TWSCSMA antenna mainly depends on seven design parameters  $f_i, l_1, R_1, R_2, r_1, G_L$ ,

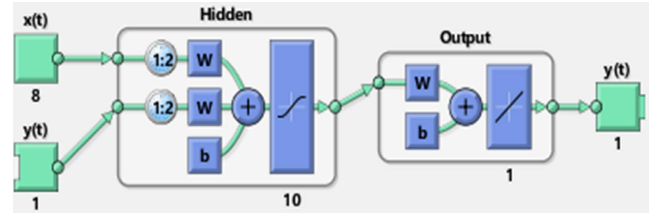


FIGURE 7. ANN architecture based on MLP.

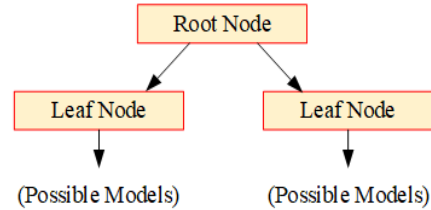


FIGURE 8. Perspective of decision tree regression.

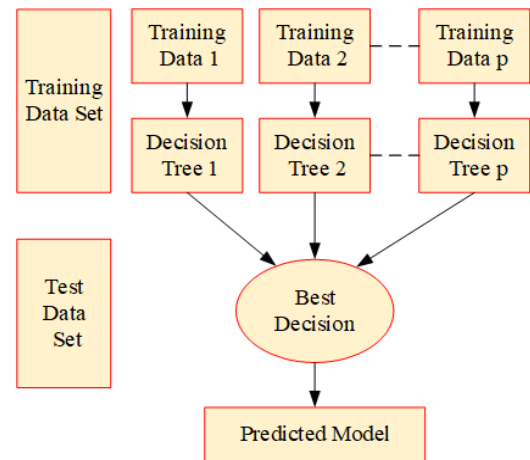


FIGURE 9. Perspective of decision forest regression.

and  $b_1$ . These seven geometric parameters act as input variables for MLR models. In the present EM simulation, 35035 samples obtained using CST Microwave Studio, give reasonably high and stable  $R^2$  values. The total sample points are collected by selecting the range of sample space of seven input parameters,  $x$  as:  $f_i \in [6.0, 6.8]$ ,  $l_1 \in [5.6, 6.4]$ ,  $R_1 \in [17.7, 18.5]$ ,  $R_2 \in [18.6, 19.4]$ ,  $r_1 \in [1.8, 2.6]$ ,  $G_L \in [7.9, 8.7]$ , and  $b_1 \in [13.6, 14.4]$  with a step size of 0.2 for each parameter. The training data is defined by  $\{ (x_i, y_i), i = 1, 2, \dots, n \}$ , where the input is  $x = (f_i, l_1, R_1, R_2, r_1, G_L, b_1)^T$ . Then the model exercises the current input samples, predicts a new parameter which is compared with the target, and calculates the prediction error as shown in Fig. 6. To search for the optimal design parameters based on the MLR model, a very fine grid over the entire sample space  $x$  with step size 0.2 mm is generated, consisting of 35035 total sample data points. Three ML regression algorithms such as: artificial neural networks (ANN), decision tree regression (DTR) and decision forest regression (DFR) [27] are used for the proposed antenna modeling and comparison of the results.

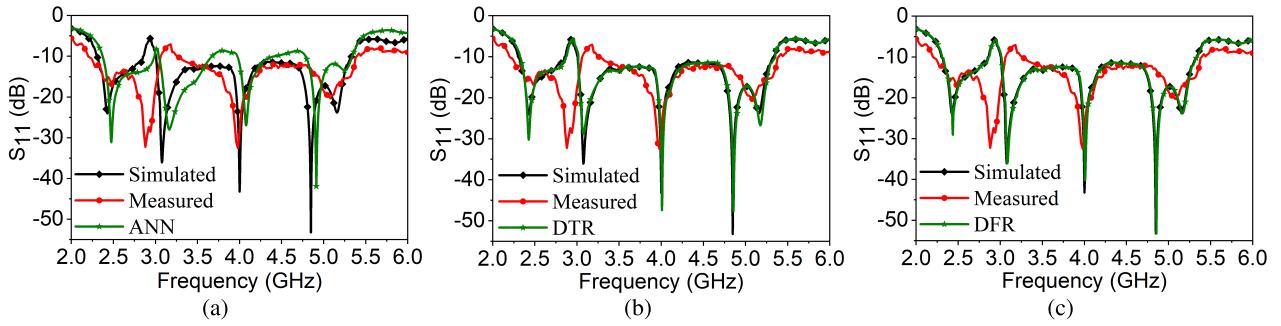


FIGURE 10. Comparison of  $S_{11}$  performance obtained from simulation, measurement and (a) ANN, (b) DTR, and (c) DFR for port 1.

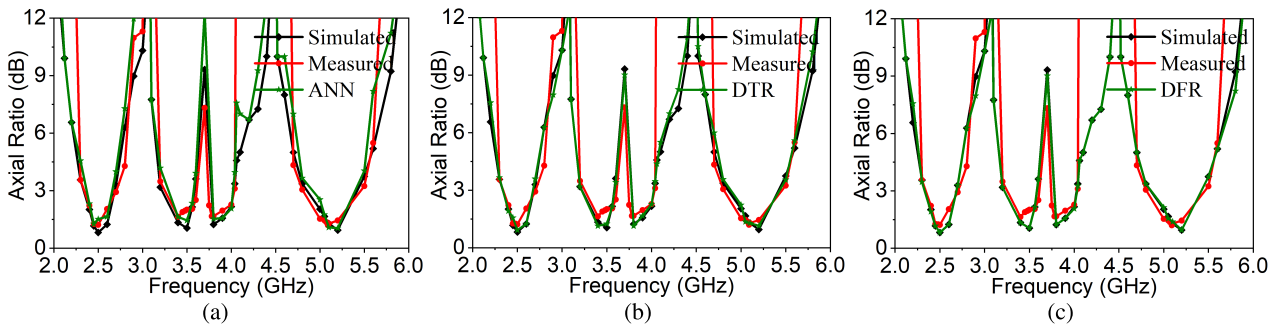


FIGURE 11. Comparison of AR of performance obtained from simulation, measurement and (a) ANN, (b) DTR, and (c) DFR for port 1.

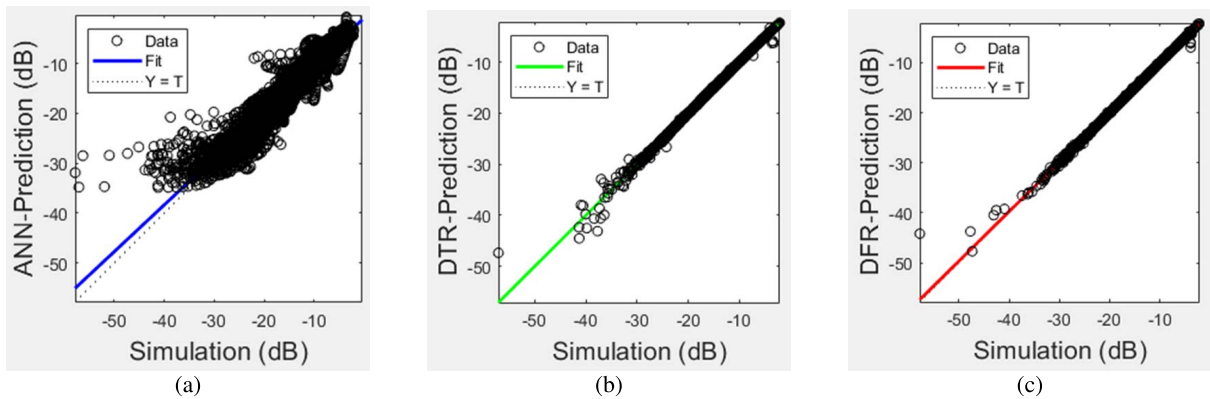


FIGURE 12. Training, testing and validation plots of regression performance of  $S_{11}$  using (a) ANN, (b) DTR, and (c) DFR for port 1.

**A. ARTIFICIAL NEURAL NETWORKS (ANN)**

ANN model is used to calculate and develop a nonlinear regression based model of biological neurons. ANN is the structure of many layers and consists of input, hidden, and output layers; each layer contains neurons. Neurons are interconnected with the corresponding links (weights). In this work, multilayer perceptrons (MLPs) is trained by Levenberg-Marquardt (LM) algorithms [28], which has the capability of fast learning and good convergence and can be expressed as:

$$x_j^{k+1} = f \left( \sum_d W_{dj}^k x_d^k + B_{bj}^k \right) \quad (14)$$

where  $W_{dj}^k$  is weighted connecting  $d^{th}$  neuron in the layer  $k$  to  $j^{th}$  neuron in layer  $k + 1$ ; which are initialized randomly.  $B_{bj}^k$  represents the bias of the  $j^{th}$  neuron in layer  $k$ . In our analysis, the data samples are divided into three parts: training data used 80% testing and validation using 10% each. The LM learning algorithm is used to develop the ANN model as shown in Fig. 7 and the neural network toolbox of MATLAB [29] is used for training the neural network.

**B. DECISION TREE REGRESSION (DTR)**

The decision tree is a regression or classification model built in the form of a tree and is also known as a predictive model [30]. In a decision tree, for predicting the class of the given

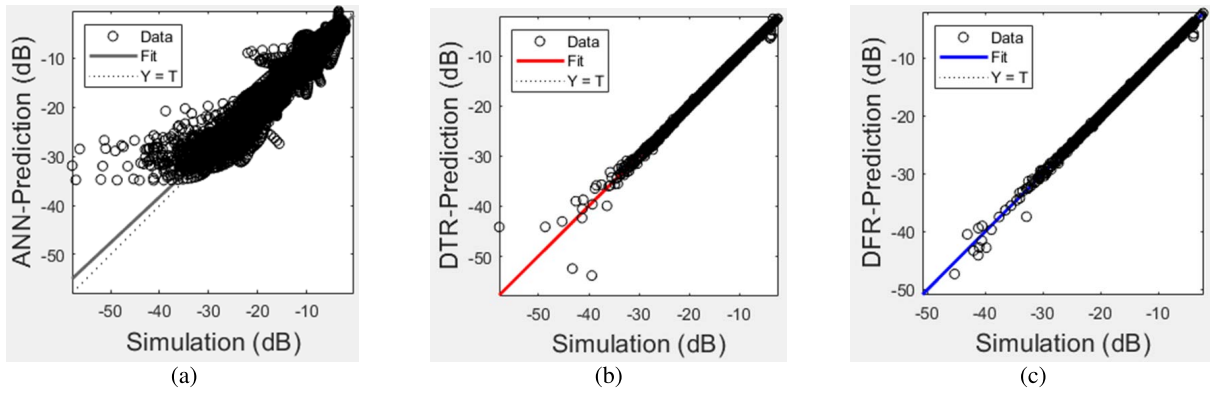


FIGURE 13. Training, testing and validation plots of regression performance of AR using (a) ANN, (b) DTR, and (c) DFR for port 1.

TABLE 2. Accuracy comparison between regression models.

Regression model	MSE	RMSE	RAE	RSE
ANN	1.892	3.017	0.922	1.026
DTR	0.036	0.487	0.022	0.026
DFR	0.049	0.237	0.029	0.069

MSE: Mean squared error. RMSE: root mean squared error. RAE: relative absolute error. RSE: relative squared error.

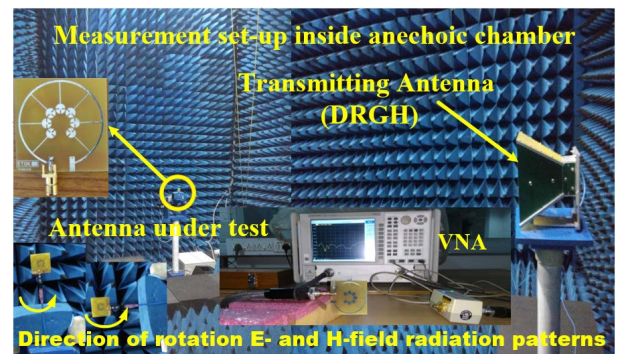
dataset, the algorithm starts from the root node of the tree. This algorithm compares the values of the root attribute with the record (real dataset) attribute and, based on the comparison, follows the branch and jumps to the next node. It is a stepwise method that optimizes the parameter values in the model and then minimizes/corrects them in the following step as shown in Fig. 8 [31]. From the figure, it is shown that the several decision trees combine and produce a better accurate model. The aim is to achieve approximation predictions that deviate from the original target and the accuracy can be expressed as a function of the mean square error (MSE) function:

$$MSE = \frac{1}{N} \sum_{i=1}^N (Y_i - \hat{Y}_i)^2 \tag{15}$$

where  $Y$  is the actual value,  $\hat{Y}$  is the prediction value and  $N$  number of data samples.

C. DECISION FOREST REGRESSION (DFR)

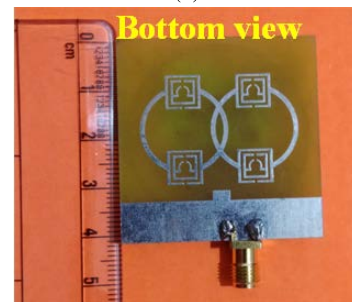
The regression model consists of an ensemble method that builds multiple decision trees and integrates their predicted models to obtain a more accurate and stable model rather than depend on an individual tree [32], [33]. Each tree in the forest learns randomly from the samples of the training data as shown in Fig. 9. In this method, a novel training data of  $\hat{x}_i, \hat{y}_i$   $_{i=1}^n$  are randomly generated from the original training data sample of  $x_i, y_i$   $_{i=1}^n$ , and have the same number of samples known as bootstrapping. In bagging, a predefined number set to  $l$  of bootstrap samples  $\hat{x}_i, \hat{y}_i$   $_{i=1}^l$  is generated according to [34], which indicates 63.2 % of the bootstrap



(a)



(b)



(c)

FIGURE 14. (a) Measurement set-up inside anechoic chamber, (b) prototype top, and (c) bottom view.

reserved sample. Hence, a decision tree algorithm is applied to each bootstrap sample of  $\hat{x}_i, \hat{y}_i$   $_{i=1}^l$  to generate  $l$  number of trees for the forest regression [35].



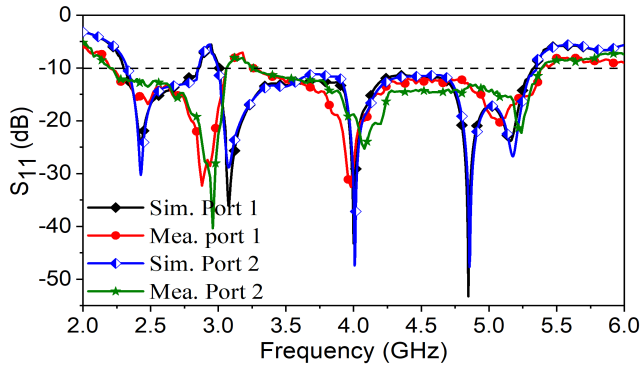


FIGURE 15. Measured and simulated  $S_{11}$  of the dual-CP TWSCSMA antenna.

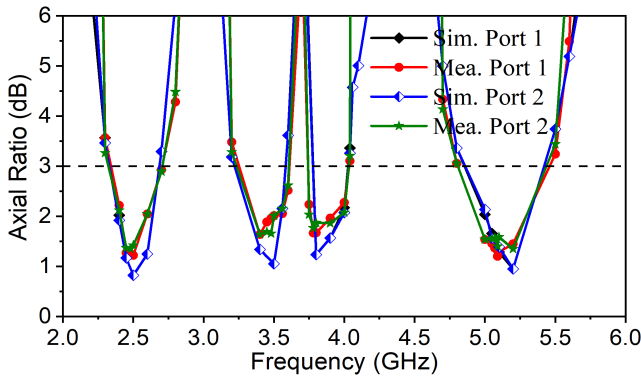


FIGURE 16. Measured and simulated AR of the dual-CP TWSCSMA antenna.

The comparison of  $S_{11}$  and AR performance of the proposed antenna obtained from EM simulation, measurement and MLR prediction models such as ANN, DTR, and DFR regression for port 1 is shown in Fig. 10 and 11 respectively. It is observed from the figures that the design accuracy parameters performance of the DTR and DFR are better than ANN and the same are depicted in Table 2. Similarly,  $S_{11}$  and AR regression performance of the proposed antenna obtained using ANN, DTR, and DFR regression models for port 1 is shown in Fig. 12 and 13 respectively. It is observed from Fig. 12 and 13, that the fit is reasonably good for all data sets, as the  $R^2$  values in the DTR and DFR 0.99 or above. In each plot of Fig. 12 and 13, the output predicted by using the fitted ANN, DTR, and DFR model has represented by the vertical axis and the true output value (simulation) is represented by the horizontal axis. From this figure, the fit line in each of these plots aligns closely with the linear regression line and the more accurate predictions for data obtained using DTR and DFR models. Hence, the regression models DTR and DFR prediction nearly the same IBW and ARBW realized from the EM simulation results compared to the ANN model.

IV. SIMULATED AND MEASURED RESULTS

To verify the design concept, the proposed antenna in Fig. 1 is fabricated and tested. The measurement set-up inside the anechoic chamber, top and bottom view of the

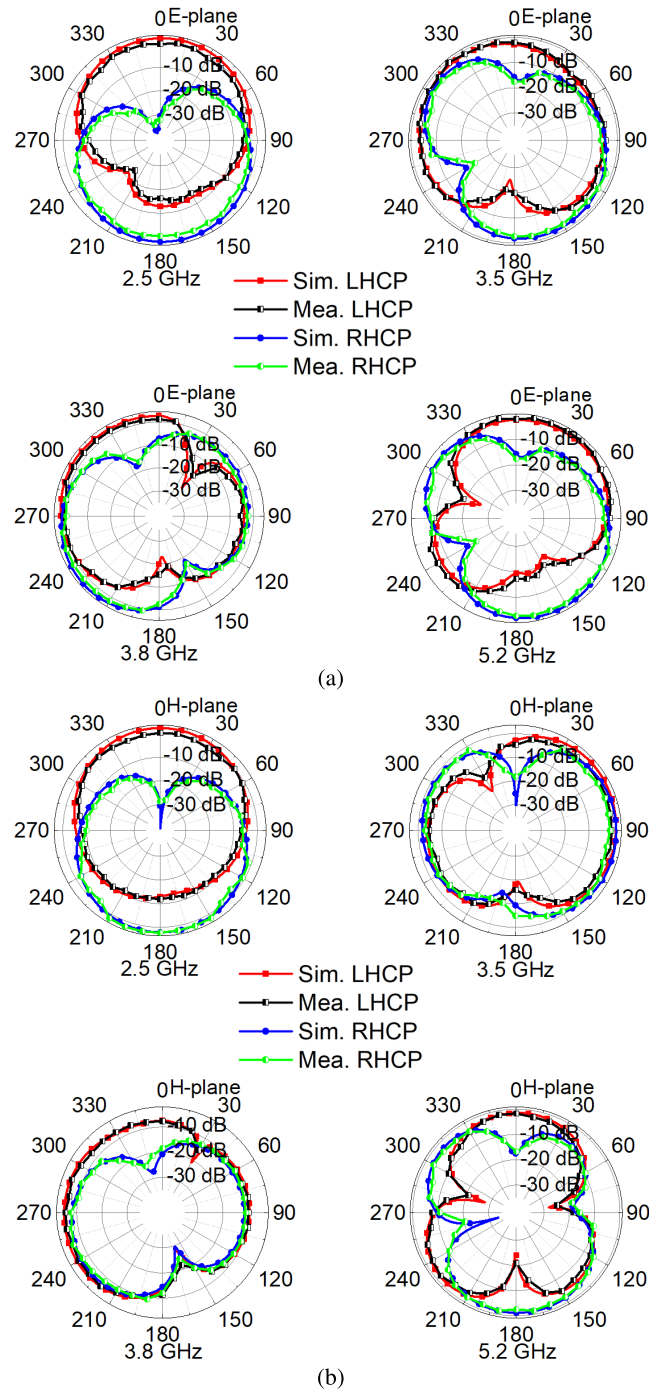


FIGURE 17. Radiation patterns at 2.5, 3.5, 3.8, and 5.2 GHz of (a) E-plane and (b) H-plane for port 1.

fabricated prototype dual-CP TWSCSMA antenna are shown in Fig. 14(a), 14(b), and 14(c), respectively. The  $S_{11}$ , AR, radiation patterns, peak gain, and efficiency are measured with an Anritsu-MS-46122B vector network analyzer (VNA) in the anechoic chamber of size:  $6 \times 4 \times 6 m^3$ .

The simulated and measured  $S_{11}$  results are depicted in Fig. 15. The measured two IBW of 33.85% (2.185–3.075 GHz) and 50.73% (3.252–5.462 GHz),  $S_{11} \leq -10$  dB have achieved for both the ports. The measured  $S_{11}$  results

TABLE 3. Comparison of multiband CP antennas.

Ref.	Feeding	Dimension (mm <sup>3</sup> )	Frequency (GHz)	IBW (%)	ARBW (%)	Peak gain (dBic)
[5]	ML	100 × 100 × 1.6	1.19-1.23, 1.56-1.58	3.7, 1.2	0.9, 0.6	1.1, 1.45
[6]	ML	70 × 70 × 1.6	2.84-3.24, 4.24-4.92	12.9, 8.5	3.1, 4.2	7.3, 8.5
[7]	ML	115 × 115 × 1.524	1.103-1.297, 1.444-1.636	16, 12.5	6.9, 0.6	2, 1.34
[8]	CP	80.8 × 80.8 × 1.52	1.12-1.69	40.57	6.56, 7.74	7.72, 8.11
[9]	MLPDN	110 × 110 × 0.8	5.0-6.2, 7.2-8.9	21, 21.2	13.2, 12.8	14.5, 17.5
[10]	ML	94.35 × 94.35 × 0.8	2.36-2.48, 3.34-3.41, 4.03-4.43	5, 2, 9.5	0.53, 0.66, 0.83	7.5, 8.7, 8.7
[11]	CP	80 × 80 × 1.6	1.16-1.18, 1.21-1.23, 1.56-1.59	2, 1.5, 2	3.4, 0.81, 0.83	5.6, 5.6, 6.3
[12]	ML	60 × 60 × 1.52	3.22-4.5, 4.76-5.98	33.16, 22.72	1.7, 3.86, 5.23	5.5, 4.63, 6.77
[13]	ML	50 × 50 × 1.56	1.48-1.87, 2.39-2.71, 3.02-3.16	21.4, 12.8, 4.5	4.37, 10.9, 3.57	2.7, 4.2, 3.5
[14]	ML	133.2 × 133.2 × 1.52	2.37-2.75, 3.4-8	14.84, 80.70	5.4, 8.3, 3.7, 2.9	5.95, 6.92, 6.37, 6.07
Proposed	ML	41 × 41 × 2.0	2.18-3.07, 3.25-5.46	33.85, 50.73	16.26, 12.52, 8.22, 13.82	2.51, 4.62, 4.32, 2.76

IBW: Impedance bandwidth. ARBW: axial ratio bandwidth. ML: microstrip line. CP: coaxial probe. MLPDN: microstrip line with power divider network.

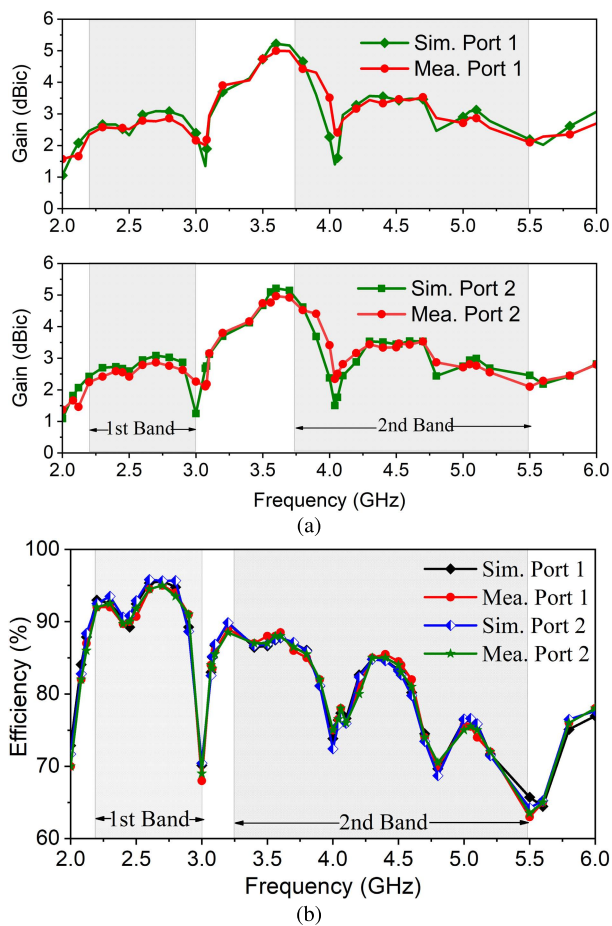


FIGURE 18. Measured and simulated the dual-CP TWSCSMA antenna (a) peak gain and (b) efficiency.

show that the first and second impedance bandwidth is shifted a little to higher frequencies than the simulated results. It is maybe due to the alignment imperfection between various

PCB layers, fabrication tolerances and SMA connector. Since the proposed antenna is symmetric in shape, the  $S_{11}$  performance is maintained within the permissible range for the feeding of ports 1 or 2.

Fig. 16 shows the simulated and measured AR of the dual-CP TWSCSMA antenna with ports 1 and 2. The results indicate that the designed antenna can maintain  $<3$  dB AR over a wide beamwidth of about  $32^\circ$ . It is seen from the figure that the measured AR for four CP bands such as 2.321–2.733 GHz (16.26%), 3.222–3.652 GHz (12.52%), 3.732–4.052 GHz (8.22%), 4.751–5.455 GHz (13.82%) at 2.5, 3.5, 3.8 and 5.2 GHz are less than 1.2 dB. Thus, measured AR characteristics validate and ensure the polarization quality of traveling-wave series-fed arrays.

Since the radiation patterns of the antenna excited either from port 1 or port 2 are similar, the measured and simulated radiation patterns for  $\phi = 0^\circ$  and  $\phi = 90^\circ$  planes at 2.5, 3.5, 3.8, and 5.2 GHz when only port 1 is excited is shown in Fig. 17. The asymmetrical antenna structure around a central axis at the feeding position (for port 1) contributes to the tilting of the radiation patterns for different frequency bands. The radiation patterns are not symmetrical at these four frequencies, however tilting is more prominent at 3.5 and 3.8 GHz. In both planes i.e., E- and H-plane, the radiation patterns are symmetrical and LHCP is stronger than RHCP by approximately 26, 14, 13, and 18 dB for 2.5, 3.5, 3.8, and 5.2 GHz respectively, in the boresight direction. The difference in the LHCP and RHCP patterns results between simulation and experiment may be due to the detector sensitivity. This confirms the satisfactory quad-band CP performance.

Fig. 18(a) shows the measured and simulated peak gain of the proposed antenna for LHCP (port 2 terminated) and RHCP (port 1 terminated) radiation. It is observed from the figure that the peak gain of the proposed antenna for both LHCP and RHCP are more or less the same. The maximum

measured peak gains are 2.51, 4.72, 4.52, and 2.86 dBic at 2.5, 3.5, 3.8, and 5.2 GHz, respectively. The measured peak gain is maintained between 2.51 and 4.72 dBic within the operational bandwidth.

For radiation efficiency measurement, first the gain  $G(\theta, \phi)$ , radiation intensity, and reflection coefficient  $\Gamma$  of the designed antenna are measured. The directivity  $D(\theta, \phi)$  is computed automatically using the radiation intensity. Using this above parameters, the antenna efficiency ( $\eta$ ) is computed using the equation given below:

$$\eta = \frac{G(\theta, \phi)}{D(\theta, \phi)}(1 - |\Gamma|^2) \quad (16)$$

The measured and simulated radiation efficiency performance is shown in Fig. 18(b). The measured efficiency from 2.2 to 5.5 GHz are about 65%–95% within the operational band and there is a small deviation in the measurement result from the simulation result due to the fabrication tolerance.

The comparison between the proposed work (TWSCSMA antenna) with other reported multi-band CP antennas are listed in Table 3. It is observed that multi-band CP antennas in [5], [6], [7], [8], [9], [10], [11], [12], [13], and [14] occupy 4.75, 2.33, 5.99, 2.95, 2.87, 2.11, 3.04, 1.62, 1.18 and 8.02 times more volume than the TWSCSMA antenna respectively. Hence, the proposed structure gives compact size among the others. Moreover, the TWSCSMA antenna has a better wide IBW and ARBW. Therefore, considering all the performance of the proposed antenna, it will be a good candidate for WiMAX and WLAN applications.

## V. CONCLUSION

A compact dual-CP TWSCSMA antenna for the WiMAX and WLAN is proposed in this work. The antenna supports a quad-band CP operation with better performance at 2.5/3.5/3.8/5.2 GHz frequency bands. The quad-band operation has been obtained by using seven series-fed circular slit array elements in an annular ring on the radiator. The two  $\leq -10$  dB IBW of 33.85% and 50.73%, four CP bands  $< 3$  dB ARBW of 16.26%, 12.52%, 8.22%, and 13.82% are achieved when the antenna is excited from port 1. The reduction in mutual coupling between the circular slit array elements is achieved by introducing SRR unit cells with double-annular rings on the defected ground plane to neutralize unwanted surface coupling waves on the radiator. MLR techniques are used to predict the accurate model performance requirements of the design parameters of the proposed antenna which will provide the best performance in terms of IBW and ARBW. And it is observed that DTR and DFR are giving better performance compared to ANN. By analyzing the simulation and experiment results, it is observed that the proposed antenna shows a compact size, better two IBW and four-CP bands than other multi-band CP antennas.

## REFERENCES

- [1] X. Jiang, Z. Zhang, Y. Li, and Z. Feng, "A low-cost wideband circularly polarized slot array with integrated feeding network and reduced height," *IEEE Antennas Wireless Propag. Lett.*, vol. 15, pp. 222–225, 2016.
- [2] S. Karamzadeh, V. Rafii, H. Saygin, and M. Kartal, "Polarisation diversity cavity back reconfigurable array antenna for C-band application," *IET Microw., Antennas Propag.*, vol. 10, no. 9, pp. 955–960, Feb. 2016.
- [3] J.-Y. Sze and S.-P. Pan, "Design of CPW-fed circularly polarized slot antenna with a miniature configuration," *IEEE Antennas Wireless Propag. Lett.*, vol. 10, pp. 1465–1468, 2011.
- [4] M. S. Wang, X.-Q. Zhu, Y.-X. Guo, and W. Wu, "Compact circularly polarized patch antenna with wide axial-ratio beamwidth," *IEEE Antennas Wireless Propag. Lett.*, vol. 17, no. 4, pp. 714–718, Apr. 2018.
- [5] W.-T. Hsieh, T.-H. Chang, and J.-F. Kiang, "Dual-band circularly polarized cavity-backed annular slot antenna for GPS receiver," *IEEE Trans. Antennas Propag.*, vol. 60, no. 4, pp. 2076–2080, Apr. 2012.
- [6] K. Kandasamy, B. Majumder, J. Mukherjee, and K. P. Ray, "Dual-band circularly polarized split ring resonators loaded square slot antenna," *IEEE Trans. Antennas Propag.*, vol. 64, no. 8, pp. 3640–3645, Aug. 2016.
- [7] Nasimuddin, Z. N. Chen, and X. Qing, "Dual-band circularly polarized S-shaped slotted patch antenna with a small frequency-ratio," *IEEE Trans. Antennas Propag.*, vol. 58, no. 6, pp. 2112–2115, Jun. 2010.
- [8] S. Lee, Y. Yang, K.-Y. Lee, and K. C. Hwang, "Dual-band circularly polarized annular slot antenna with a lumped inductor for GPS application," *IEEE Trans. Antennas Propag.*, vol. 68, no. 12, pp. 8197–8202, Dec. 2020.
- [9] C. X. Mao, S. Gao, Y. Wang, Q. X. Chu, and X. X. Yang, "Dual-band circularly polarized shared-aperture array for C/X-band satellite communications," *IEEE Trans. Antennas Propag.*, vol. 65, no. 10, pp. 5171–5178, Oct. 2017.
- [10] Q. Tan and F.-C. Chen, "Triband circularly polarized antenna using a single patch," *IEEE Antennas Wireless Propag. Lett.*, vol. 19, no. 12, pp. 2013–2017, Dec. 2020.
- [11] O. P. Falade, M. U. Rehman, Y. Gao, X. Chen, and C. G. Parini, "Single feed stacked patch circular polarized antenna for triple band GPS receivers," *IEEE Trans. Antennas Propag.*, vol. 60, no. 10, pp. 4479–4484, Oct. 2012.
- [12] J. G. Baek and K. C. Hwang, "Triple-band unidirectional circularly polarized hexagonal slot antenna with multiple L-shaped slits," *IEEE Trans. Antennas Propag.*, vol. 61, no. 9, pp. 4831–4835, Sep. 2013.
- [13] P. M. Paul, K. Kandasamy, and M. S. Sharawi, "A triband circularly polarized strip and SRR-loaded slot antenna," *IEEE Trans. Antennas Propag.*, vol. 66, no. 10, pp. 5569–5573, Oct. 2018.
- [14] T. V. Hoang, T. T. Le, Q. Y. Li, and H. C. Park, "Quad-band circularly polarized antenna for 2.4/5.3/5.8-GHz WLAN and 3.5-GHz WiMAX applications," *IEEE Antennas Wireless Propag. Lett.*, vol. 15, pp. 1032–1035, 2016.
- [15] D. J. Bisharat, S. Liao, and Q. Xue, "Wideband unidirectional circularly polarized antenna with L-shaped radiator structure," *IEEE Antennas Wireless Propag. Lett.*, vol. 16, pp. 12–15, 2017.
- [16] V. Rafii, J. Nourinia, C. Ghobadi, J. Pourahmadazar, and B. S. Virdee, "Broadband circularly polarized slot antenna array using sequentially rotated technique for C-band applications," *IEEE Antennas Wireless Propag. Lett.*, vol. 12, pp. 128–131, 2013.
- [17] Q. Luo, S. Gao, M. Sobhy, J. T. S. Sumantyo, J. Li, G. Wei, J. Xu, and C. Wu, "Dual circularly polarized equilateral triangular patch array," *IEEE Trans. Antennas Propag.*, vol. 64, no. 6, pp. 2255–2262, Jun. 2016.
- [18] Y. Shen, S.-G. Zhou, G.-L. Huang, and T.-H. Chio, "A compact dual circularly polarized microstrip patch array with interlaced sequentially rotated feed," *IEEE Trans. Antennas Propag.*, vol. 64, no. 11, pp. 4933–4936, Nov. 2016.
- [19] Y. Qasaymeh, A. Almuhasien, and K. Issa, "Design of compact dual circularly polarized ring series-fed quasi-lumped antenna array," *Prog. Electromagn. Res.*, vol. 103, pp. 111–121, 2020.
- [20] C. A. Balanis, *Antenna Theory: Analysis and Design*, 4th ed. Hoboken, NJ, USA: Wiley, 2016.
- [21] D. M. Pozar, "RCS reduction for a microstrip antenna using a normally biased ferrite substrate," *IEEE Microw. Guided Wave Lett.*, vol. 2, no. 5, pp. 196–198, May 1992.
- [22] Y. X. Guo, L. Bian, and X. Q. Shi, "Broadband circularly polarized annular-ring microstrip antenna," *IEEE Trans. Antennas Propag.*, vol. 57, no. 8, pp. 2474–2477, Aug. 2009.
- [23] Y. F. Lin, H. M. Chen, and S. C. Lin, "A new coupling mechanism for circularly polarized annular-ring patch antenna," *IEEE Trans. Antennas Propag.*, vol. 56, no. 1, pp. 11–16, Jan. 2008.
- [24] A. Ishikawa, T. Tanaka, and S. Kawata, "Frequency dependence of the magnetic response of split-ring resonators," *J. Opt. Soc. Amer. B, Opt. Phys.*, vol. 24, no. 3, pp. 510–515, Mar. 2007.

- [25] Q. Wu, Y. Cao, H. Wang, and W. Hong, "Machine-learning-assisted optimization and its application to antenna designs: Opportunities and challenges," *China Commun.*, vol. 17, no. 4, pp. 152–164, Apr. 2020.
- [26] Q. Wu, H. Wang, and W. Hong, "Multistage collaborative machine learning and its application to antenna modeling and optimization," *IEEE Trans. Antennas Propag.*, vol. 68, no. 5, pp. 3397–3409, May 2020.
- [27] W. Y. Al-Rashdan and A. Tahat, "A comparative performance evaluation of machine learning algorithms for fingerprinting based localization in DM-MIMO wireless systems relying on big data techniques," *IEEE Access*, vol. 8, pp. 109522–109534, 2020.
- [28] M. T. Hagan and M. B. Menhaj, "Training feedforward networks with the Marquardt algorithm," *IEEE Trans. Neural Netw.*, vol. 5, no. 6, pp. 989–993, Nov. 1994.
- [29] H. Demuth and M. Beale, "Neural network toolbox for use with MATLAB-user's guide version 4.0," MathWorks, Natick, MA, USA, Tech. Rep., 2004.
- [30] R. S. Millan-Castillo, E. Morgado, and R. Goya-Esteban, "On the use of decision tree regression for predicting vibration frequency response of handheld probes," *IEEE Sensors J.*, vol. 20, no. 8, pp. 4120–4130, Apr. 2020.
- [31] T. M. Mitchell, *Machine Learning*. New York, NY, USA: McGraw-Hill, 1997.
- [32] L. Rokach, "Decision forest: Twenty years of research," *Inf. Fusion*, vol. 27, pp. 111–125, Jan. 2016.
- [33] M. N. Adnan and M. Z. Islam, "Forest PA : Constructing a decision forest by penalizing attributes used in previous trees," *Expert Syst. Appl.*, vol. 89, pp. 389–403, Dec. 2017.
- [34] J. Han, J. Pei, and M. Kamber, *Data Mining: Concepts and Techniques*. San Mateo, CA, USA: Morgan Kaufmann, 2006.
- [35] L. Breiman, J. Friedman, R. Olshen, and R. Stone, "Classification and regression trees," in *Regression Trees*. Boca Raton, FL, USA: CRC Press, 2017, pp. 216–265.



**BUDHADEB MAITY** was born in Odisha, India, in 1980. He received the B.E. degree in electronics and telecommunication engineering from the Biju Patnaik University of Technology, Rourkela, India, in 2004, and the M.Tech. degree in RF and microwave engineering from IIT Kharagpur, Kharagpur, India, in 2012. He is currently pursuing the Ph.D. degree with IIT Guwahati, Guwahati, India. His current research interests include compact UWB CP antenna, UWB harmonic suppression antenna, multiband antenna using ML, and microwave and RF circuits.



**SISIR KUMAR NAYAK** (Senior Member, IEEE) received the B.E. degree in electrical engineering from the University College of Engineering, Burla, India, in 1999, and the master's and Ph.D. degrees in electrical engineering from the Indian Institute of Science, Bengaluru, India, in 2003 and 2009, respectively. He was a Postdoctoral Research Fellow at the Division of Electromagnetics, School of Electrical Engineering, KTH Royal Institute of Technology, Stockholm, Sweden. He is currently a Professor with the Department of Electronics and Electrical Engineering, IIT Guwahati, Guwahati, India. His research interests include integration of renewable sources with the grid, WPT systems, pulsed power systems, and high-voltage engineering. He is also a reviewer of several IEEE TRANSACTIONS and journals.

...